Supplement of Ann. Geophys., 43, 633–649, 2025 https://doi.org/10.5194/angeo-43-633-2025-supplement © Author(s) 2025. CC BY 4.0 License.





Supplement of

$Toolkit\ for\ incoherent\ scatter\ radar\ experiment\ design\ and\ applications\ to\ EISCAT_3D$

Spencer Mark Hatch et al.

Correspondence to: Spencer Mark Hatch (spencer.hatch@uib.no)

The copyright of individual parts of the supplement might differ from the article licence.

S1 Supplementary information

Here we provide both a range resolution diagnostic figure (Figure S1) and 2D histograms of GEMINI vs. reconstructed convection velocity components (Figure S2). These figures are referenced in the main text in the description of the first example experiment (Section 5.1) and second example experiment (Section 5.2), respectively.

5 S1.1 Range resolution diagnostic plot

10

Figure S1 shows a typical diagnostic figure used for selecting an ideal range resolution for the first example experiment presented in Section 5.1 of the main article. Panel a is identical to Figure 3a in the main text, except that the first beam is highlighted in orange. As in Figure 3 of the main text, the center column shows results for winter conditions and the right column results for summer conditions.

For winter conditions, Figure S1b1 shows the uncertainty of the magnetic eastward convection component as a function of altitude on the y axis as well as modulation bit length $\Delta r_{\rm mod}$ (lower x axis) and lag spacing $\Delta \tau$ (upper x axis) for a constant range gate resolution of 15 km over 180-km to 400-km altitude. The uncertainty averaged over all altitudes is shown in Figure S1c1. The lowest average uncertainty as a function of altitude occurs for $5 \text{ km} \lesssim \Delta r_{\rm mod} \lesssim 10 \text{ km}$.

Corresponding quantities for summer conditions are shown in Figures S1b2 and S1c2. From the latter figure it is clear that the average uncertainty minimizes near $\Delta r_{\rm mod} = 2.5$ km.

These results motivation our selection of $\Delta r_{\rm mod} = 5$ km for winter conditions and $\Delta r_{\rm mod} = 2.5$ km for summer conditions in Section 5.1 of the main text.

S1.2 2D histograms of GEMINI vs. reconstructed convection velocity components

Figure S2 shows heatmaps of original versus reconstructed eastward (d–f), northward (g–i), and upward (j–l) velocity components for the three beam patterns shown in Figure 4. These heatmaps indicate that for all beam patterns the reconstructed convection velocities are generally within a few tens of m/s of the original convection velocities. Differences between the various beam patterns are mostly negligible but nevertheless visible.

Results in this figure reinforce the conclusion in the main manuscript that the goal of the second example experiment in Section 5.2 (reconstruction of the ionospheric convection pattern with as little overall residual error as possible) is approximately equally well achieved by all three beam patterns.

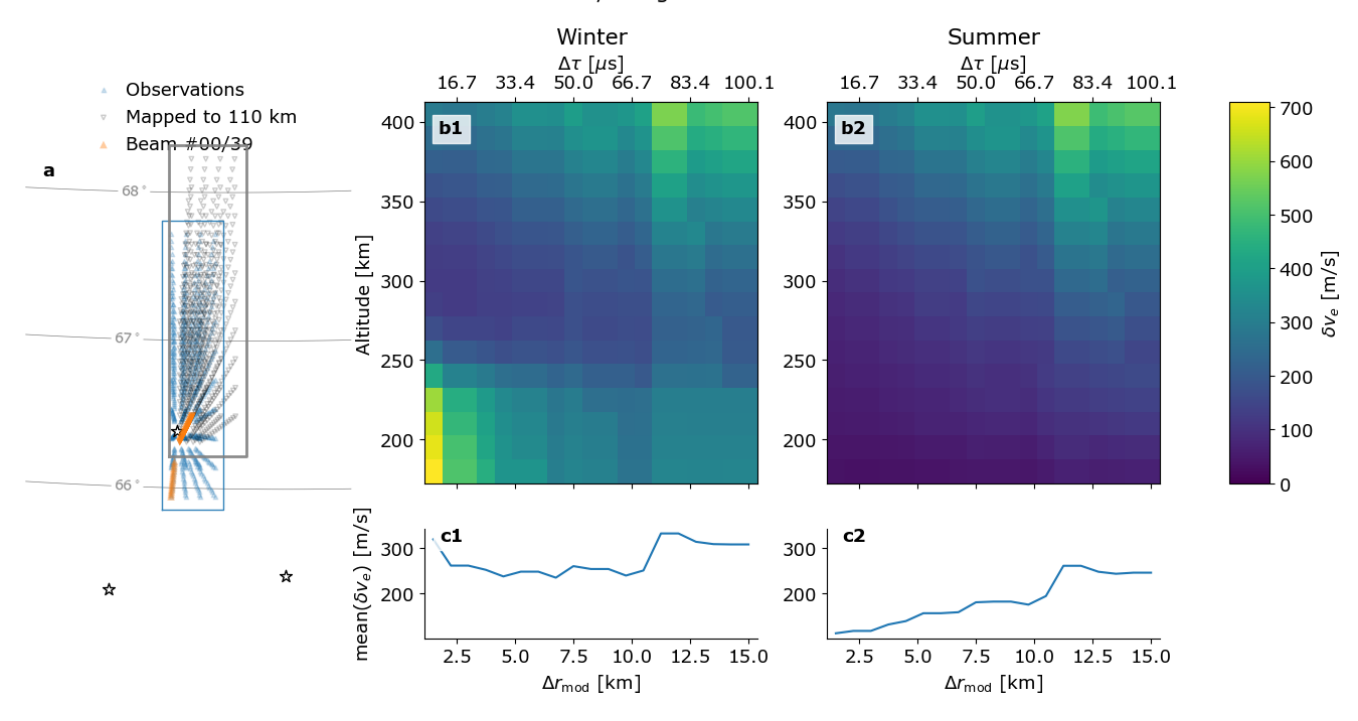


Figure S1. Example diagnostic figure used for selecting range resolution values in the first example experiment, with results for winter and summer conditions shown in the center and right columns, respectively. a: Beam pattern layout in the same format as Figure 3a of the main article, with locations of observations made between 180- and 400-km altitude at intervals of 15 km shown as blue triangles, and their locations after mapping along geomagnetic field lines to 110-km altitude as black triangles. The extent of the observation region before and after mapping is indicated by the blue and gray boxes, respectively. b1-b2: Uncertainty of magnetic eastward convection as a function of altitude on the y axis as well as modulation bit length $\Delta r_{\rm mod}$ (lower x axis) and lag spacing $\Delta \tau$ (upper x axis). c1-c2: Uncertainty of magnetic eastward convection averaged over all altitudes.

References

Reistad, J. P., Hatch, S. M., Laundal, K. M., Oksavik, K., Zettergren, M. D., Vanhamäki, H., and Virtanen, I. I.: Volumetric reconstruction of ionospheric electric currents from tri-static incoherent scatter radar measurements, ESS Open Archive, 2024.

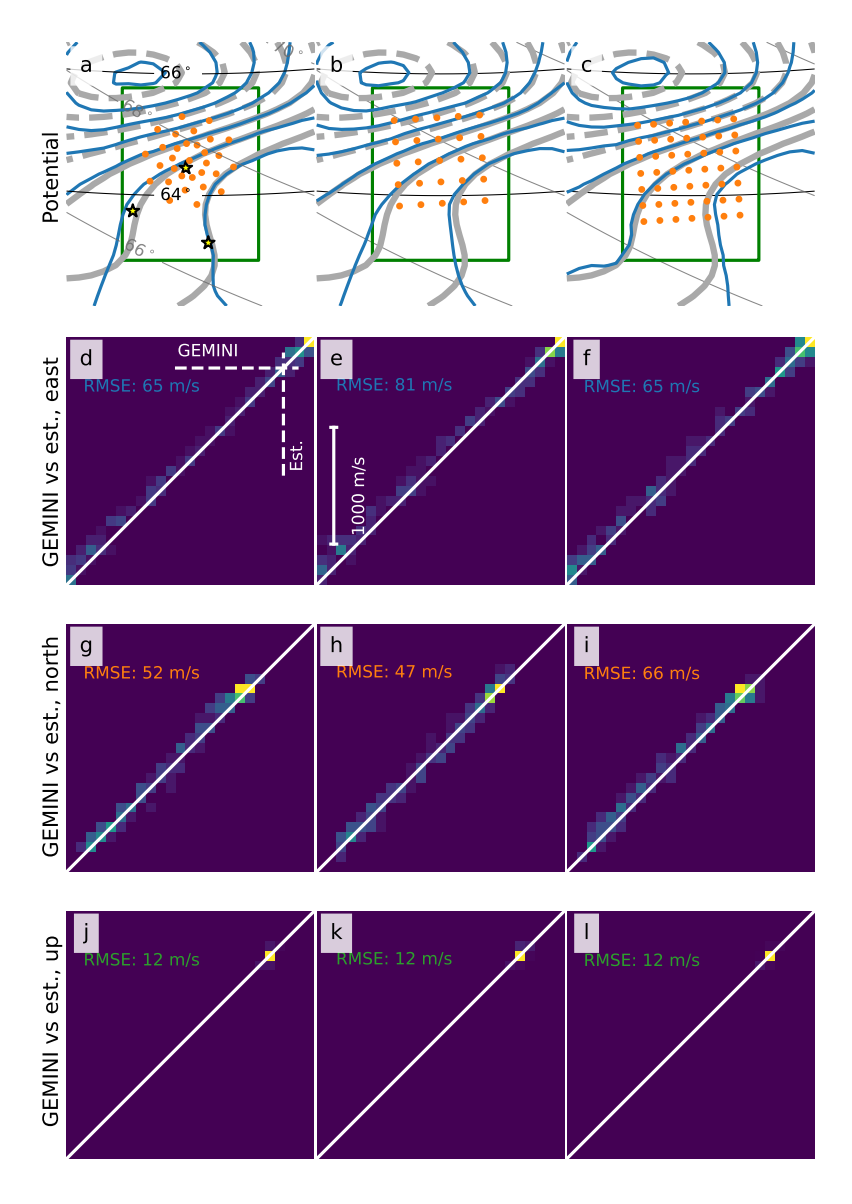


Figure S2. Reconstruction of ionospheric potential for the three different beam patterns shown in Figure 4 (from left to right): the Reistad et al. (2024) beam pattern, and 25- and 47-beam patterns covering respectively $\sim 160 \text{ km}^2$ and $\sim 180 \text{ km}^2$. **a-c:** Original and reconstructed ionospheric potential patterns (thick gray lines and thin blue lines, respectively), identical to those shown in Figures 4a-c in the main article. **d-f:** Reconstructed eastward convection plotted against true convection (y and x axes, respectively). **g-i:** Reconstructed northward convection plotted against true convection. **j-l:** Reconstructed upward convection plotted against true convection.